Applied Soft Computing 114 (2022) 108100

Contents lists available at ScienceDirect

Applied Soft Computing

journal homepage: www.elsevier.com/locate/asoc

Optimum aeroelastic control via iterative neural network training for wind-resistant cyber–physical buildings

Khalid M. Abdelaziz *, Jared D. Hobeck

Alan Levin Department of Mechanical and Nuclear Engineering, Kansas State University, Manhattan, KS, USA

GRAPHICAL ABSTRACT

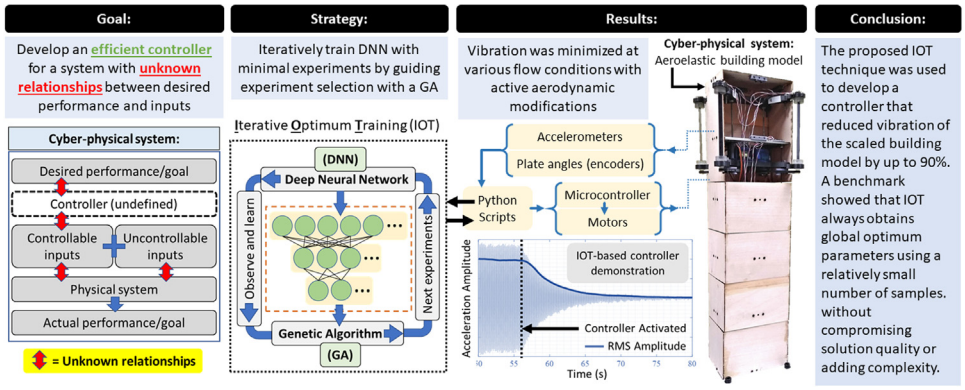

ARTICLE INFO

Article history:
Received 27 May 2021
Received in revised form 14 September 2021
Accepted 26 October 2021
Available online 22 November 2021

Keywords:
Deep learning
Cyber–physical systems
Expensive optimization
Distributed aerodynamic actuators
Wind-induced vibration

ABSTRACT

This research presents iterative optimum training (IOT), which integrates deep neural networks (DNNs) and population-based optimization techniques such as genetic algorithms (GAs). The proposed technique reduces the number of experiments needed for training without adding complexity compared with non-iterative DNN-GA techniques commonly used in the literature. In this work, IOT is used to train an optimal controller for minimizing wind-induced vibration (WIV) using distributed aerodynamic actuators. Wind tunnel experiments of a scaled cyber–physical aeroelastic building model are used to demonstrate a novel application of the technique. IOT trains a DNN to approximate building vibration at different wind conditions and actuator orientations using an initial set of experiments. After this initial training, a GA uses the DNN to predict actuator orientations that minimize WIV for the given wind condition. A group containing best orientations from the GA and uniform random orientations is used to perform additional experiments and training of the DNN to enhance exploitation and exploration. This process is repeated until the stopping criteria is achieved. This paper includes results of a benchmark study comparing IOT to GA and DNN-GA techniques. Experimental results show that IOT-based online control of the aeroelastic model reduces WIV acceleration amplitudes by up to 90% within 9.8 s upon controller activation.

1. Introduction

Fluid flow around bluff bodies such as tall buildings and structures can cause a number of fluid–solid-interaction phenomena, e.g., turbulent buffeting, flutter and vortex shedding [1]. The occurrence of one or a combination of these phenomena ultimately results in wind-induced fluctuating forces that cause structural vibration [2,3]. Various works in the literature, including previous work of the authors, establish that modifications to the perimeter geometry of a building can have a profound effect on its wind-induced vibration (WIV) response [4–6]. Elshaer et al. [7] performed a simulation-based aerodynamic corner optimization and reported up to a 30% reduction in the drag coefficient, which leads to a reduction in vibration amplitudes [7]. Sharma et al. [4] concluded that even minor corner modifications to the

* Corresponding author.
E-mail address: abdelazizk@ksu.edu (K.M. Abdelaziz).

https://doi.org/10.1016/j.asoc.2021.108100
1568-4946/

List of abbreviations

ANN	Artificial neural network
AOA	Angle of attack
CAARC	Commonwealth aeronautical advisory research committee
DAA	Distributed aerodynamic actuators
DNN	Deep neural network
DOE	Design of experiments
DOF	Degree of freedom
ELU	Exponential linear unit
FE	Finite element
GAs	Genetic algorithms
IOT	Iterative optimum training
LDV	Laser doppler vibrometer
MLP	Multi-layer perceptron
PSD	Power spectral density
RMS	Root mean square
SA	Simulated annealing
WIV	Wind-induced vibration

building (e.g., corner rounding, chamfering) can result in 30%–60% reduction in wind-induced loads [4]. However, such modifications may also have adverse effects when subjected to different wind flow characteristics and surrounding environments, which may result from erection of other structures in the vicinity [4,8,9]. Xie and Yang [10] presented a case study of a 270 m-high building with plate fairings attached to its corners at a fixed orientation of 45° [10]. The authors reported an 18% reduction on structural design wind loads as a result. Yang et al. [11] studied buildings with various vertical plate configurations on their perimeter. The authors reported as much as 50% decrease in the drag force coefficient for certain configurations [11]. These studies establish the effectiveness of minor passive aerodynamic modifications in WIV control for tall buildings. It is also shown that different flow characteristics and environments require different modifications to maintain reduced WIV and prevent adverse effects. This calls for the development of dynamic or active aerodynamic modifications.

Evaluating the effect of active aerodynamic modifications is challenging for computational simulations because they normally require repetitive reconstruction of the simulation model, which is computationally expensive [12]. Previous work of the authors used a simplified 2D fluid–solid-interaction simulation model, which enabled the geometry to change without reconstruction in order to more efficiently optimize a smart morphing façade system consisting of four corner plates [6,13]. These corner plates were actively controlled based on average wind conditions. The authors reported a 60%–80% reduction in WIV amplitudes when the controller was employed. This 2D simplification also introduced considerable approximation into the model, especially regarding turbulence modeling and 3D flow effects. In the literature, cyber–physical experimental wind tunnel models have recently been used to design aerodynamic modifications for aviation and tall building applications at a reduced experimental cost [14–16]. In the current study, a cyber–physical scaled building model is used to implement online controller training in a wind tunnel. The model has four actively controlled corner plates, similar to the previous simulation-based study of the authors [6,13]. The plates function as distributed aerodynamic actuators (DAAs), which the controller can independently position in response to time-averaged measurements of the wind condition to minimize the resulting building vibration.

The core component of the proposed control scheme is a multi-layer perceptron (MLP) DNN that approximates the relationships between the inputs (average wind conditions and DAA orientations) and the outputs (building accelerations). These relationships are difficult to predict because they display strong nonlinearity and non-monotonicity where, in certain conditions, small changes to the geometry can cause large changes to the wind-building system [6,13]. Many physical systems can display such behavior, which calls for the development of methods to model, optimize and control them. Population-based optimization techniques (e.g., GAs, particle swarm, ant colony, etc.) are widely used in the literature because they typically do not require special knowledge of the system being optimized (e.g., mathematical form, derivatives, etc.). These techniques are also known to consume a large number of experiments or simulations, which may be impractical for many reasons including excessive monetary and/or time requirements. Methods are developed in the literature to tackle such *expensive optimization* problems, including both population-based and direct methods [17];[18]. The basic concept is to consume the least possible number of function evaluations even at the expense of increased computational overhead of the method itself [19]. However, these methods usually focus on optimizing the system rather than generating a prediction model for it, which is needed in the current study to perform online DAA control [20]. As discussed in later sections, this work uses genetic algorithms (GAs) and deep neural networks (DNNs) to perform both functions simultaneously, while using the DNN as a surrogate model to guide the dispatch of additional function evaluations.

Genetic algorithms are inspired by biological genetic process found in nature. They have been used with great success in many studies in the literature [12,21]. This optimization strategy is generally able to operate on discontinuous and multimodal systems; however, GAs typically require a large number of experiments. Artificial neural networks (ANNs) are inspired by the operation of the human brain. DNNs are ANNs that have more than one hidden layer between the input and the output layers. They are widely utilized in performing cognitive functions (e.g., image recognition and speech recognition) normally performed by humans as well as predicting and controlling the behavior of physical systems [22]. DNNs are widely integrated with GAs in the literature to reduce the number of experiments required for optimization. Initial experiments are used to train an MLP DNN that predicts the system behavior. The GAs then dispatch the predictor MLP instead of requiring additional experiments, thus greatly reducing the overall experiments required. Dasgupta et al. [23] utilized this technique to model and optimize a polymer-enhanced ultrafiltration system [23]. Márquez-Nolasco et al. [24] also used the technique to optimize and estimate the thermal energy of an absorber with graphite disks [24]. Conde-Gutiérrez et al. [25] used a similar technique to optimize an absorption heat transformer [25]. In these works, the experiments performed for training the MLP are arbitrary and unguided, except by human experience. This may pose a problem for an arbitrary complex system whose behavior is not completely understood, because there is no guarantee that these experiments will train the MLP DNN so it can render a result sufficiently close to the global optimum. For such systems, a simple 'grid' of experiments may not be adequate or efficient because highly nonlinear areas of the parameter domain may need to be more densely probed relative to other areas.

The research presented here uses a concept called *optimization-guided training* to overcome the previously discussed drawbacks [19]. The main strategy of this approach is to perform the experiments selectively based on the progression of the optimization instead of randomly or based on a grid of the parameters. This

approach serves two purposes: (1) the training can be performed with a smaller number of experiments and (2) the resulting MLP is more densely trained around the optimum operating control parameters. Point (2) is especially relevant for optimally controlling a system because control parameters providing for better system performance are prioritized in the training, which increases the likelihood of generalizing the *optimum modes* of performance for the system. Optimization-guided training is realized in this work by an iterative modification to the original MLP-GA procedure referred to here as iterative optimum training (IOT). At first, a relatively small initial set of experiments is used to train the MLP. The GA operates using the MLP instead of requiring additional experiments. A set of best solutions from the GA are evaluated using additional experiments and added to the training data set to improve the training around the current optima to enhance exploitation. Similarly, another set of uniformly random solutions are evaluated and added to the data set to enhance exploration. The expanded data set is used to retrain the MLP which is used again by the GA. The process is repeated until the stopping criteria are met. Each iteration only requires a small number of experiments, relative to the initial experiments, to evaluate the solutions obtained from the GA. Because IOT starts from a smaller initial sample set, it may locate the global optimum by using significantly fewer experiments. Also, because the training data set is expanded with random samples at each iteration, IOT does not rely on the initial sample being representative of the whole domain, so it has no inherent stall mechanism (as opposed to pure GAs). In the proposed framework, the GA can be replaced by any other population-based optimization technique (e.g., particle swarm, ant colony, etc.) to benefit from the iterative nature of the training. Huang et al. [26] used a similar iteration technique to optimize the thickness of blow molded parts [26]. In that work, the authors expand the data set by only one sample obtained from the GA optimization after each iteration without adding random samples. Therefore, the choice of this one sample is more critical for the progression of the search, so the authors (1) used design of experiments (DOE) to obtain the initial sample set as a non-iterative exploration mechanism and (2) integrated GAs and simulated annealing (SA) to improve the local search ability of the GA to enhance exploitation. In the current study, multiple samples are added from the GA and at random to enhance both exploitation and exploration, which simplifies the implementation. Additionally, the current study uses the technique for online training of a data-driven optimum controller and evaluates the technique by comparing it to others using a benchmark function.

The generated controller uses the trained MLP to predict the system performance and select the DAA orientations that minimize WIV at different average wind conditions. Another optimizer MLP maintains a direct correlation between the wind condition and the optimum DAA orientations. This improves response time of the online controller because it does not have to search the predictor MLP for each wind condition it encounters. The data-driven nature of the generated WIV controller enables it to be trained for an arbitrary number of control surfaces on many types of structures. While demonstrating the adaptation capabilities of the proposed controller is outside the scope of this work, predictor-optimizer ANN-based controllers are known in the literature to have such capabilities [27]. Adaptation will enable the controller to respond to changes in the environment, such as erection of adjacent buildings.

Section 2 of this paper provides a definition of the optimization and training problem posed by using DAAs to minimize WIV and presents the IOT technique developed in this work. Section 3 discusses the scaled aeroelastic building model and the wind-tunnel experiments. Section 4 presents the WIV minimization results for the scaled building model and the MLP prediction performance. Lastly, Section 5 includes a summary and conclusions along with a brief discussion of related current and future work that is being pursued by the authors.

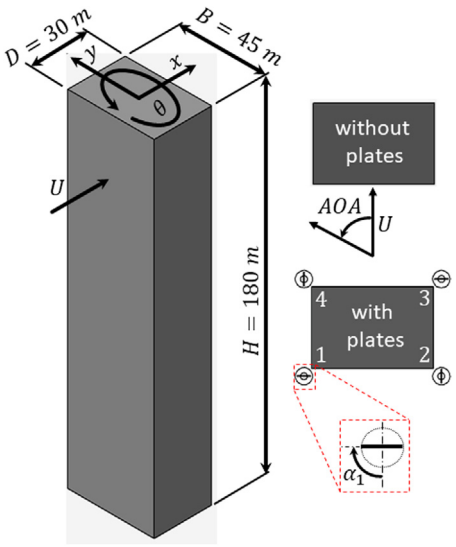

Fig. 1. Schematic of the standard CAARC building with four corner plates showing all parameters relevant to this study.

2. Problem statement and methods

This section begins by introducing the physical system that originally motivated the research. It continues with a discussion of the approach taken to minimize WIV using DAAs, and includes details about the IOT technique, numerical benchmark comparisons, and development of an IOT-based controller.

2.1. Problem definition

The Commonwealth Aeronautical Advisory Research Committee (CAARC) standard building is used as a base case in this work because it is thoroughly studied in the literature [8,28]. Fig. 1 illustrates the full-scale CAARC building along with all key parameters including dimensions which are 180 × 45 × 30 m (Height H × Width B × Depth D). As illustrated in Fig. 1, the building exhibits two sway (bending) and 1 torsional (twisting) vibration degrees of freedom (DOFs) that are of primary interest for this study. The figure also shows a top view of the building with four plates acting as the DAAs attached at the corners having orientation angles ($\alpha_1 \ldots \alpha_4$). Since flow separation is strong at the corners, varying the plate orientations at these locations is expected to have a significant effect on WIV. This choice is also motivated by findings of previous work of the authors [6,13]. This study uses a 1:400-scale aeroelastic model of the CAARC building for experimental validation. The height and longitudinal placement of the plates in addition to other design details of the scaled aeroelastic model are discussed in Section 3.

The primary function of the controller is to obtain plate angle combinations that minimize WIV accelerations at different average wind conditions. The objective function for this optimization problem can be expressed as,

$$Min.Q\left(\overline{w}, \alpha_i\right) = RMS\left(\ddot{x}\right) + RMS\left(\ddot{y}\right) + \frac{B}{2} RMS\left(\ddot{\theta}\right) \quad (1)$$

where α_i are the plate angles between 0 and 180 degrees, subscript i denotes the plate number, $\overline{w} = f\left(\overline{U}, AOA\right)$ is the time-averaged wind condition which consists of the average wind speed $\overline{U}$ and the angle of attack AOA, RMS is the root-mean-square for a defined interval of acceleration readings, and $\ddot{x}$, $\ddot{y}$, $\ddot{\theta}$ are the along-wind sway, cross-wind sway and torsional accelerations, respectively. The RMS of $\ddot{\theta}$ has units of rad/s^2 as opposed

to m/s^2 for the sway components, so it is numerically scaled by half of the building width, which represents the radius of twist. The range of 0 to 180 degrees for α_i is sufficient because the corner plates are aerodynamically symmetric. If nonsymmetric DAAs are used, then a 360 degree range should be considered. Approximating the function in Eq. (1) is essential for the proper operation of an online controller that minimizes it. Even though the building acceleration response depends on both the wind condition and the plate angles, only the latter can be manipulated by the controller. This separates the optimization parameters into uncontrollable ($\overline{w}$) and controllable parameters (α_i).

2.2. Iterative optimum training

Fig. 2 illustrates the MLP network used by the IOT procedure to approximate Eq. (1), Q ($\overline{w}, \alpha_i$). The hidden layers of the network contain neurons using exponential linear unit (ELU) activation functions defined as,

$$ELU\,(x) = \begin{cases} x & x \geq 0 \\ e^x - 1 & x < 0 \end{cases} \tag{2}$$

due to their low computational cost and proven performance [29]. The output of the MLP network is a sigmoid activation function ($\sigma\,(x) = 1/\{1 + e^{-x}\}$) because its result is scaled between 0.0 and 1.0, which is suitable for representing all potential values of Eq. (1).

Fig. 3 is a flow chart illustrating the IOT procedure. For each wind condition, initial training for the MLP is performed using k initial experiments. The GA utilizes the trained MLP rather than requiring additional experiments (inverse ANN). The best $r_1 \times k$ solutions found by the GA are evaluated using additional experiments, where r_1 is the GA expansion ratio. If the stopping criteria are met, the procedure terminates for the current wind condition $\overline{w}_j$. Otherwise, additional experiments are also performed for $r_2 \times k$ uniform random samples, where r_2 is the random expansion ratio. The original samples k are expanded by the summation of the new samples $(r_1 + r_2)\,k$. The MLP is retrained using the expanded set of samples and the process repeats until stopping criteria are met. The way in which the original samples k are expanded after each iteration greatly affects the performance of the IOT technique. The $r_1 \times k$ solutions found by the GA help improve future training accuracy around the current optima, which represents an exploitation mechanism, while the $r_2 \times k$ additional random solutions prevent the IOT technique from stalling if the initial samples k had no representation of the global optimum solution, which represents an exploration mechanism. The next section discusses how these two mechanisms improve the solution quality and reduce the number of experiments required to perform optimum training. In addition to generating the trained MLP $\hat{Q}\,(\overline{w}, \alpha_i)$, the procedure also stores the optimum plate angle combinations $[\alpha_i]_j^*$ associated with each wind condition encountered during training. These plate angles are used to initiate the controller as illustrated in Section 2.4.

2.3. Numerical benchmark study

This section uses a benchmark function to provide comparisons to other techniques and establish the training/optimization performance gains associated with the IOT technique. The Alpine 2 function was used to test, develop, and compare the IOT technique before using it with actual wind tunnel experiments [31]. This function was chosen mainly because it is multimodal and non-separable. This behavior is expected in the wind-plate-building system because the wake forming behind a plate significantly affects the plate behind it, which causes non-separability. The Alpine 2 function is given as [31],

$$Q\,(X) = Q\,(x_1, \ldots, x_p) = \prod_{i=1}^{p} \sqrt{x_i} \sin\,(x_i) \tag{3}$$

where p is the number of dimensions and $x_i \in [1, 10]$. The function is continuous and has a global maximum $f\,(X^*) = 2.808^p$ at $x_i = 7.917$.

Table 1 lists parameters of the compared online training techniques, including the developed IOT technique. The first technique considered is a direct GA that does not train or utilize an MLP. The GA generation size was varied among 62 different values, as shown in Table 1. For each generation size, 30 independent trials were performed. The maximum number of generations for

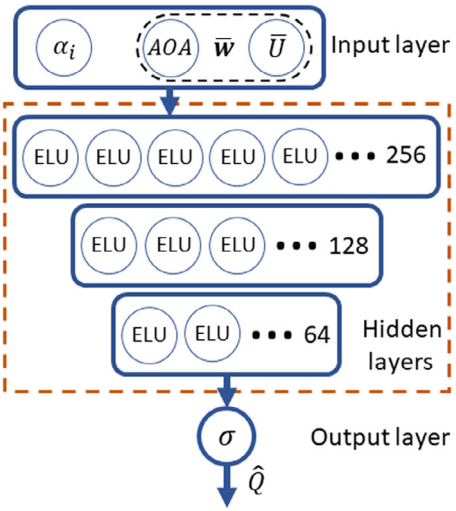

Fig. 2. The MLP $\hat{Q}\,(\overline{w}, \alpha_i)$ network used to implement the IOT procedure.

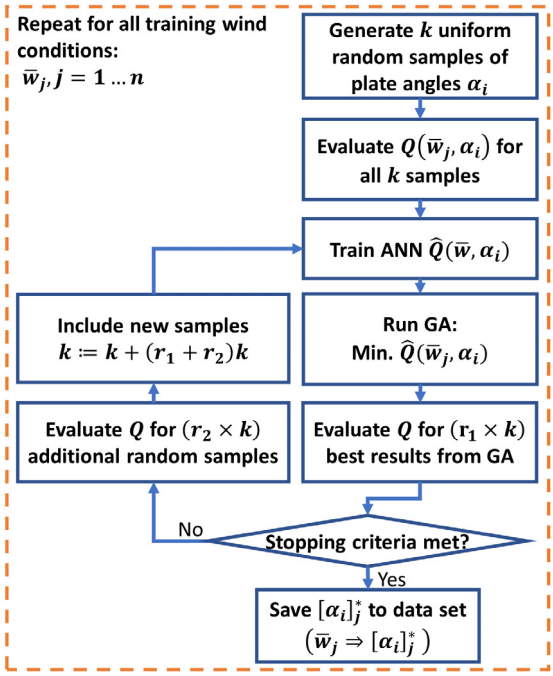

Fig. 3. Flow chart of the IOT technique for minimizing Eq. (1) while simultaneously training the MLP.

Table 1
Parameters of the compared techniques.

Parameter	GA	MLP-GA	IOT (this work)
Dimensions p	4		
Selection method	Fitness proportionate (roulette wheel)		
Crossover	Single point, 80%		
Mutation	Uniform, 10%		
Elitism	12.5% of population		
Training samples	N/A	[64, 72 … 4088, 4096]	[64, 72 … 504, 512]
Population	[16, 24 … 504, 512]	1024	
Generations	50	50	20
MLP architecture	N/A	Same as Fig. 2, but neuron counts are 512, 256, 128 to fit larger sample counts of benchmark	
MLP training	N/A	Backpropagation using Adam algorithm [30]	
Optimum fitness	$2.808^4 = 62.17$		
Expansion ratios	N/A	N/A	$r_1 = r_2 = 25\%$
Stopping criterion	$Q \geq 59.10$ (95% × 62.17)	N/A (no iteration)	$Q \geq 59.10$(95% × 62.17)
Normalized objective	$\frac{Q - Min.}{Max. - Min.} = \frac{Q - (-62.17)}{2 \times 62.17}$		

each trial was set at 50 to prevent a stalling GA from halting the progress of the comparison. The second technique considered was a GA that utilizes an MLP (MLP-GA) that is trained from a constant number of samples without iteration, similar to several studies in the literature [23–25]. The training sample size was varied among 504 different values, as shown in Table 1. For each sample size, 6 independent trials were performed. Finally, the IOT technique developed in this work and illustrated in the previous section was compared to the other techniques. In reference to Fig. 3, all parameters $x_1 \ldots x_p$ are assumed controllable, so $n = 1$. The initial sample size k was varied among 56 different initial sample sizes, as shown in the table. For each initial sample size, 24 independent trials were performed. At each iteration, the sample size was expanded by 25% using the best solutions from the GA that uses the trained MLP and by another 25% using uniform random samples ($r_1 = r_2 = 0.25$ in Fig. 3). Except for the iterative modification, all MLP architecture and training parameters are identical among MLP-GA and IOT. The stopping criterion and all other parameters of the three techniques are listed in Table 1. The generation size and number of samples and/or trials for each technique were determined to obtain a fair comparison between the total number of samples required by each technique. This is evident in Fig. 4, which plots the total number of samples versus the normalized objective function (explained in Table 1) for all three techniques. In many instances, the GA technique is shown to achieve low normalized objective values (0.7–0.8) at a relatively low number of samples (<2000). This behavior seems to decrease as the number of samples increases until it disappears at ∼4000 samples. This indicates stalled GA runs, in which the initial population fails to contain a representation of the global optimum solution. The MLP-GA technique shows a large variance of the obtained optima at small sample sizes. That variance decreases as the sample size increases. Additionally, the mean normalized objective obtained by MLP-GA only manages to match the GA technique at ∼2800 samples and the IOT technique at ∼3500 samples. These drawbacks of MLP-GA happen because small sample sizes tend to fail to produce an MLP whose prediction correctly represents the behavior function around the global optimum. The IOT technique presented in this work has the means to alleviate these drawbacks. At each iteration, when the stopping criterion is not met, the original sample k is expanded in light of previous iterations as well as with additional random samples. This causes the IOT technique to have no stall mechanism such as the case with the GA technique; therefore, the IOT solution always satisfies the stopping criterion shown in Fig. 4. Also, because the IOT starts from a small initial sample k, it can still satisfy the stopping criterion early when smaller samples manage to properly train the MLP. These observations explain that the IOT fitted curve consistently provides the best normalized objective for the total number of samples consumed.

2.4. IOT-based controller

As illustrated in Section 2.2, The IOT procedure has two outputs: (1) the dataset of the optimum plate angles α_i^* and (2) the trained predictor MLP $\hat{Q}(\overline{w}, \alpha_i)$. Fig. 5 illustrates a controller which utilizes these outputs to perform steady-state control of the wind-building-plates system Q (Eq. (1)). An optimizer MLP $\alpha_i^*(\overline{w})$ is used directly by the controller to obtain the optimum plate angles knowing the current average wind condition. The IOT output #1 mentioned earlier is used to provide initial training for the optimizer MLP. During operation, the measured building accelerations, the corresponding average wind conditions, and the plate angles can be used to continuously train the predictor MLP. The background optimizer uses output #2 (the predictor MLP itself) to search for plate angles $\widehat{\alpha_i^*}$ that provide best expected performance for the current average wind condition (inverse MLP). The background optimizer does not have to be dispatched for every wind condition that the system encounters; therefore, it can operate locally using any remaining computational capacity, or remotely on separate computational machines. The plate angles found by the background optimizer and the corresponding average wind condition can be used to continuously train the optimizer MLP.

3. Aeroelastic model

This section discusses the scaled aeroelastic model and implementation of the IOT experimental training procedure. The aeroelastic model has a dimensional scale of 1:400. Table 2 lists the scaling parameters of other quantities, which were required to ensure transferability to the full-scale building [32]. As will be shown in Section 3.4, the damping ratios were approximately the same as the full-scale building, which yields the unity scale for the Scruton number and eventually the accelerations, as shown in the table [28].

The standard CAARC building discussed in Section 1 has an average mass density of 160 kg/m^3 which is uniformly distributed along its height [8]. Also, it is reported that four lumped masses

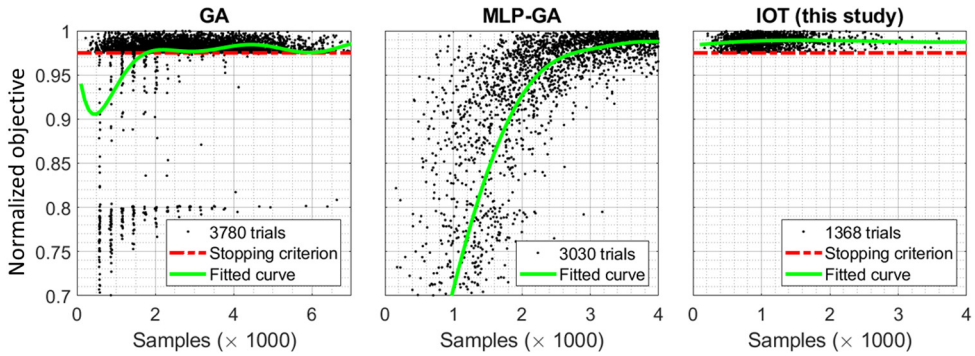

Fig. 4. Performance comparisons of the tested online training techniques.

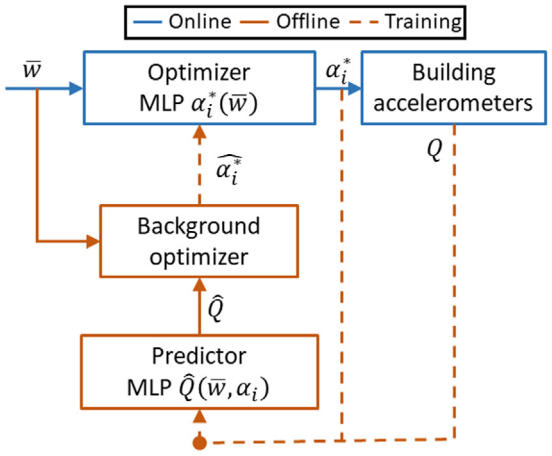

Fig. 5. IOT-based control architecture for wind-building-plate system.

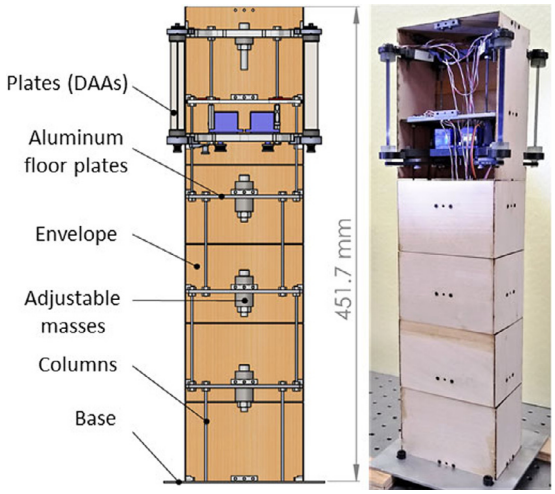

Fig. 6. Illustration and photo of the 1:400 scaled aeroelastic CAARC building model used in this study.

Table 2
Dynamic similarity parameters for the scaled aeroelastic model (subscripts m = model and f = full-scale building).

Quantity	Parameter	Scale value
Length	$\lambda_L = l_m/l_f$	1/400
Frequency	$\lambda_f = f_m/f_f$	33
Time	$\lambda_t = t_m/t_f$	1/33
Displacement	$\lambda_L = l_m/l_f$	1/400
Mass	$\lambda_m = m_m/m_f$	$1/400^3$
Velocity	$\lambda_v = \lambda_L\lambda_f$	1/12.1
Damping ratio	$\zeta_m = \zeta_f$	1
Acceleration	$a_m = a_f$	1

are enough to study most tall buildings [32]. Fig. 6 illustrates details of the 1:400 scale aeroelastic CAARC model. The height of the scaled model is 451.7 mm. Four aluminum plates representing the floors were equally spaced along the height (451.7/5 = 90.3 mm). In order to evenly distribute wind forces, the amount of mass at each floor was proportional to the envelope height assigned to it. The top floor was assigned double the envelope height of other floors to make room in the mass budget for the DAA plates and their control mechanisms. This resulted in a model with four adjustable lumped masses representing five floors two of which were combined at the top floor. The columns were cut from 6061 aluminum threaded rods and were attached to the floors using self-locking nuts. The envelope of the model was composed of balsa wood panels laser cut from 1/32" (0.8 mm) stock and attached to the floors. The weight of the final model excluding the base was 0.62 kg, which was 2% over the target weight of 0.61 kg.

3.1. GA-assisted aeroelastic model design

For the standard CAARC building, the first order sway mode shapes are linear along the height of the building, while the torsional mode shape is uniform. The torsional/sway first order natural frequency ratio ranges from 1.2–1.5 in the literature [8, 33]. Column diameters at each floor were used to manipulate the mode shapes and frequency ratios of the model [33]. A GA optimization procedure was formulated and used to determine the column cross-sections that (1) minimize the deviation from linear mode shapes and (2) obtain appropriate torsional/sway frequency ratios. The objective of this optimization was defined as,

$$min.f\ (d_i) = \sum_{i=1}^{4} \Delta_i + \left| \frac{\omega_\theta}{\omega_x} - 1.2 \right| \tag{4}$$

where d_i are the column diameters for floors $i = 1$ to 4, which were chosen from a discrete list of readily available off-the-shelf diameters, Δ_i is the deviation from the linear mode shape at floor i, ω_θ and ω_x are the torsional and along-wind sway natural frequencies respectively. A finite element (FE) model of the scaled building was used to calculate Eq. (4). The model consisted of ~300,000 nodes for ~160,000 3D solid elements and accounted for every component of the aeroelastic model assembly including fasteners, hardware, and the envelope boards. The mass density of each component was estimated during the initial design phase and updated with measured values after components were acquired prior to assembly. The FE model was created using the

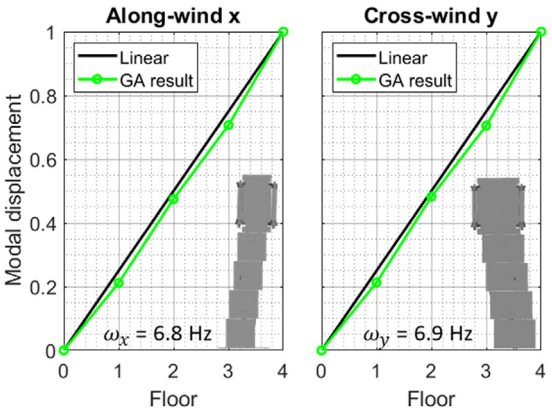

Fig. 7. First order sway mode shapes for the scaled aeroelastic model obtained using GA optimization.

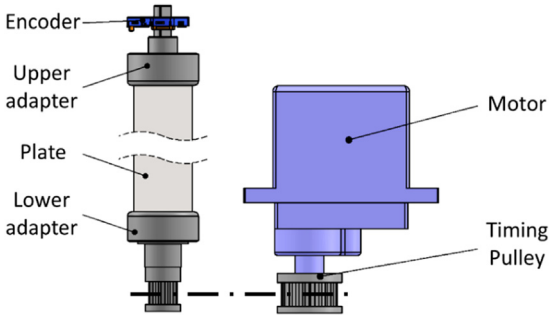

Fig. 8. Components of the rotating plates mechanism.

Solidworks® frequency analysis module. Fig. 7 illustrates the first order sway mode shapes and natural frequencies (ω_x and ω_y) obtained using the GA optimization. The mode shapes show very little deviation from linearity. These deviations are primarily due to limiting the column diameter selection to discrete sizes. The torsional mode shape occurs at 8.0 Hz, so the torsional/sway ratio is 1.17 and 1.16 for the along- and cross-wind sway directions. This ratio is only 2.5% lower than the range of ratios found in the literature [28].

3.2. Distributed aerodynamic actuators

The four DAA plates were cut from 0.8 × 12.8 mm steel to a length of 90 mm each. The width of the plates was chosen to be approximately 10% of the building width B to ensure practical plate dimensions at the full scale. The plates extended for approximately 20% of the total building height to maintain their rigidity. They were placed towards the top of the model to maximize their effect because this is where wind velocities, wind forces, and building deflections are typically the largest. Fig. 8 illustrates the plate rotation mechanism. Each plate attaches to a rotational encoder at the top, which measures actual plate position. The plate motors have a range of 0–180° and weigh ∼9 grams each. They can perform full travel in ∼0.2 s with a stall torque of ∼0.1 N.m and are compatible with Arduino®.

3.3. Cyber–physical instrumentation

Fig. 9 illustrates the data acquisition and plate control instrumentation that were used to complete the full cyber–physical system. Python scripts utilized the nidaqmx software library to control the data acquisition unit and enable serial communication with an Arduino which was used to control the motors.

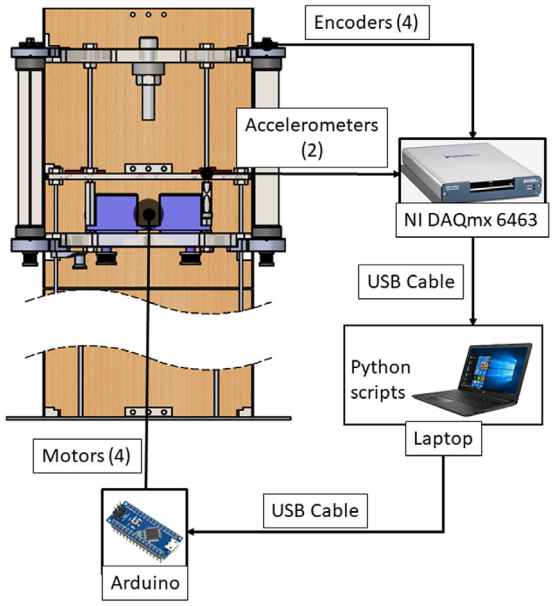

Fig. 9. Cyber–physical instrumentation consisting of data collection and plate control systems.

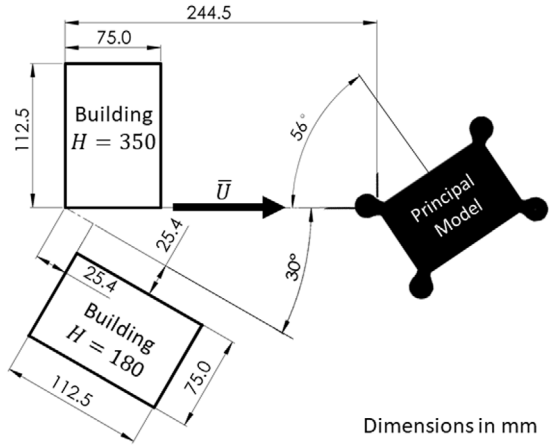

Fig. 10. Layout of the upstream buildings added to increase the RMS accelerations at the diagonal critical direction ($AOA = 56°$).

The tests were performed in a mobile wind tunnel built by the Kansas State University Wind Power Team. The tunnel has a 1.1 m × 1.1 m test section powered by 4 industrial fans each measuring 0.5 m × 0.5 m. The tunnel generates wind speeds ranging from 0–14 m/s. The speed control on the tunnel is open-loop and human operated with discrete integer 'level' settings. Average free-stream windspeed $\overline{U}$ was determined using 3-min averaged readings with a Testo 405i hot-wire anemometer placed ∼200 mm upstream of the model. While all wind speed readings are taken at a single point, the 3-min averaging generates distinct average wind speed values for each tunnel speed setting, which is necessary for controller training.

3.4. Characterization

Experiments were performed to determine the first mode natural frequencies and damping ratios for the scaled model. The model was given an initial displacement smaller than 3 mm and left to vibrate freely while the motion was measured with a Polytec® OFV-5000 laser doppler vibrometer (LDV) unit as well

Table 3
List of frequency and damping ratios for the scaled model.

Parameter	Design	Actual	Difference
Natural frequency ratios			
ω_θ/ω_x	8.0 Hz/ 6.8 Hz = 1.17	7.4 Hz/ 6.5 Hz = 1.13	3.4%
ω_θ/ω_y	8.0 Hz/ 6.9 Hz = 1.16	7.4 Hz/ 6.7 Hz = 1.10	5.2%
Damping ratios			
ζ_x	1%	1.1%	10%
ζ_y	1%	1%	0.3%
ζ_θ	–	0.8%	–

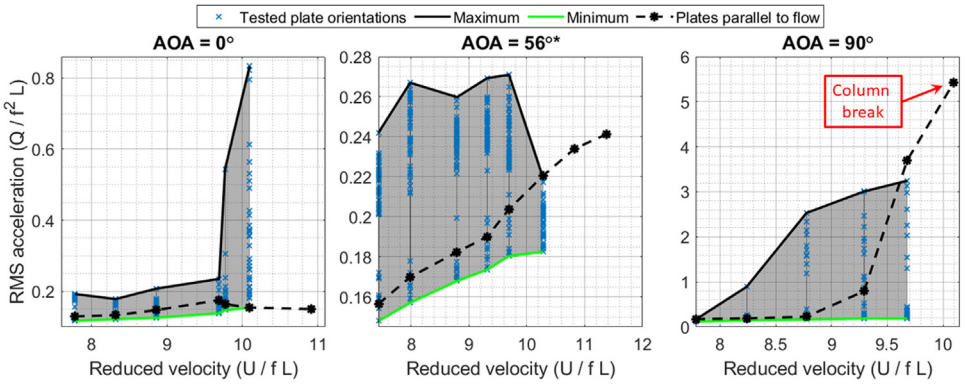

Fig. 11. RMS acceleration trends for all tested wind conditions obtained after two IOT iterations ($\star$ with the upstream buildings illustrated in Fig. 10).

as the onboard accelerometers. The power spectral density (PSD) charts were plotted for each DOF to obtain natural frequencies. Damping ratios were estimated using the logarithmic decrement method. Table 3 lists the characterization results which show minimal deviation from the design natural frequency ratios as explained in Section 3.1. These small deviations were primarily due to minor manufacturing and assembly inaccuracies. The obtained damping ratios for the linear modes are also in line with the full-scale model, so no special modifications were made to change the damping ratios.

3.5. Experiment-based training

This section summarizes the wind tunnel training process for the DAA controller, which follows the IOT technique discussed in Section 2. The system was trained at three critical wind directions (AOA): 0°, 56° (diagonal) and 90°. The RMS accelerations (Eq. (1)) observed for $AOA = 56°$ were considerably lower than those for $AOA = 0°$ and 90°, which coincides with findings in the literature [28]. Given such low accelerations, controller performance could not be demonstrated at that direction. Therefore, a special case was considered only for $AOA = 56°$ where two rigid scaled building models were positioned upstream of the principal model as illustrated in Fig. 10. The presence of these upstream buildings created additional flow features (e.g., vortices and large-scale turbulence), which increased principal model accelerations thereby enabling demonstration of the DAA controller. A total of 9 average wind speeds were tested at each wind direction, so a total of 27 distinct wind conditions $\overline{w}$ were used for training. The wind speed values for each wind direction are illustrated in Fig. 11.

In reference to Fig. 3, Table 4 lists the IOT technique parameters that were employed in the wind tunnel training process. Two iterations were used as a stopping criterion because it was observed that the RMS reduction is negligible thereafter. These parameters translate to 60 experiments per wind condition, which equals ∼1620 experiments in total for the 27 wind conditions considered. The experiment control program is provided with a different list of plate angle combinations to test at each wind condition. For each combination, the acceleration data is collected for 2 min and written to a comma-separated file. The files from all combinations are later post-processed to extract the RMS accelerations (Eq. (1)) and continue the IOT procedure.

Table 4
IOT technique parameters employed for the wind tunnel training process.

Parameter	n	k	r_1	r_2	Iterations
Value	27	40	12.5%	12.5%	2

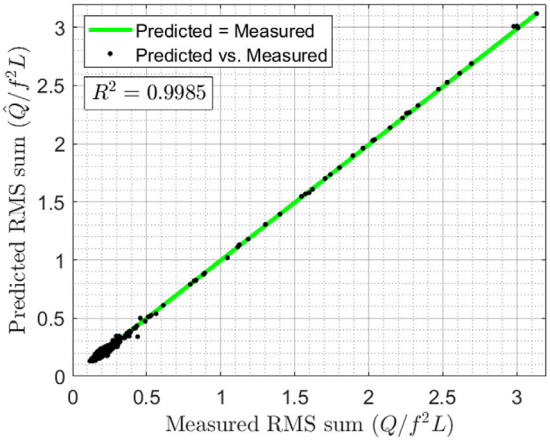

Fig. 12. RMS acceleration prediction performance of the MLP trained using the IOT procedure.

4. Results and discussion

This section discusses the performance of an IOT-based controller from observations of wind tunnel experiments, seeking to actively minimize RMS acceleration of an aeroelastic model via optimal control of DAAs. A brief consideration of the expected real-life performance of the cyber–physical system is also included.

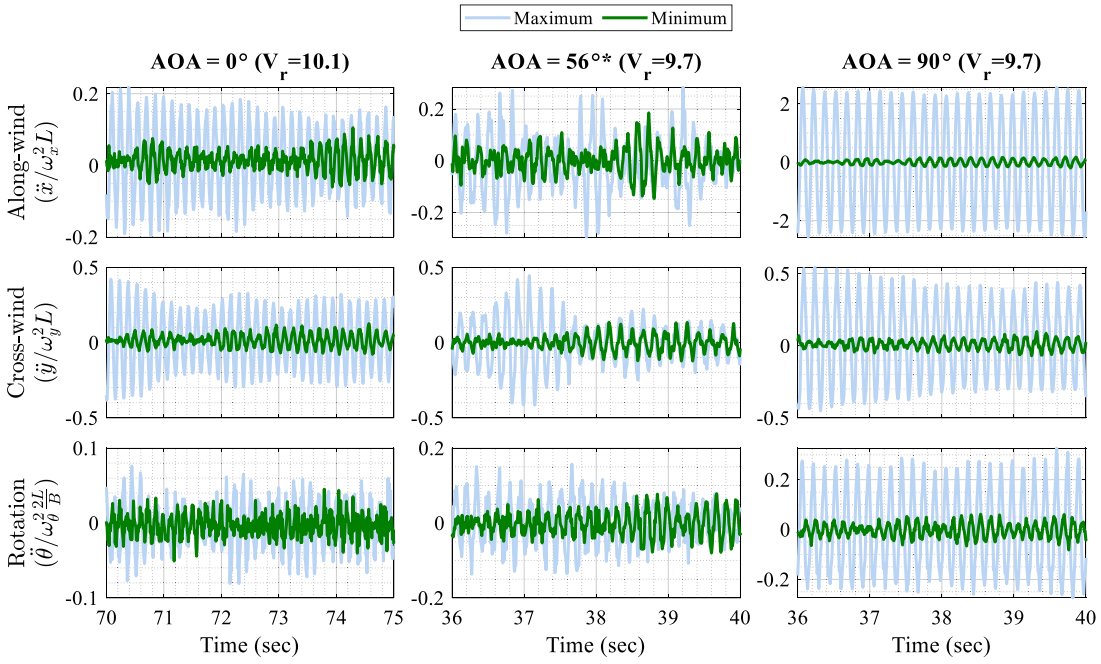

Fig. 13. A sample of time histories showing maximum (blue) and minimum (green) building acceleration responses to demonstrate the influence of IOT-based DAA control (⋆ case with upstream buildings as illustrated in Fig. 10).

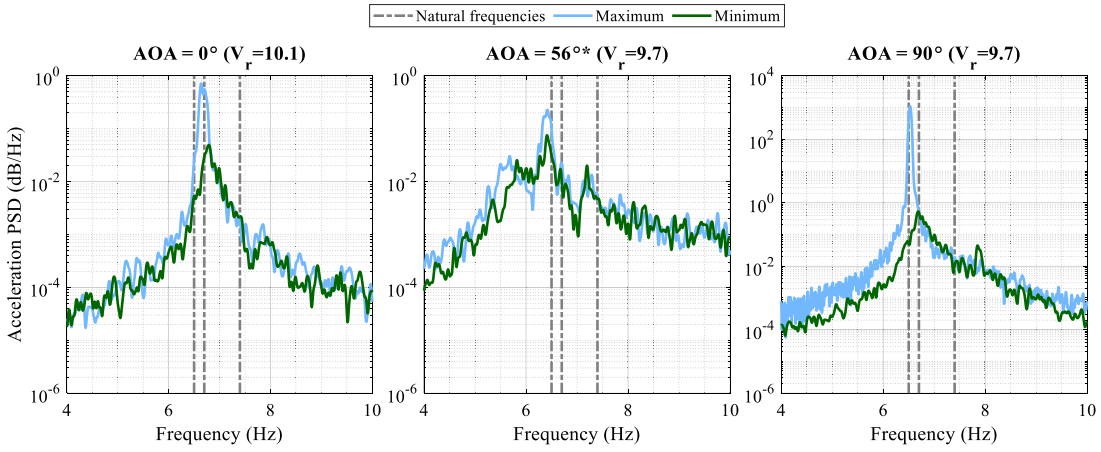

Fig. 14. Comparison between along-wind acceleration PSDs of best (green) and worst (blue) plate configurations for the three wind directions considered (⋆ case with upstream buildings as illustrated in Fig. 10).

4.1. IOT performance

Fig. 11 plots the sum of RMS acceleration (Eq. (1)) in a normalized form (Q/f^2L) versus the reduced velocity ($V_r = \overline{U}/fL$) for the tested wind conditions. Where Q is the RMS acceleration sum (Eq. (1)), f is the along-wind sway natural frequency, L is the length scale ($L = \sqrt{DB}$) and $\overline{U}$ is the average wind speed. To isolate the effect of the plates, the figure also plots the neutral condition considered when the plates are parallel to the flow for minimum engagement. For $AOA = 0°$, the neutral position was found to generate relatively low RMS values, but some plate orientations maximized the RMS response considerably at $V_r \geq 9.7$. The best obtained plate orientations after two iterations are always at or below the neutral position, which indicates the effectiveness of the IOT optimization procedure. A similar trend is obtained at $AOA = 56°$ (with upstream buildings shown in Fig. 10), but the neutral RMS response increases with V_r until the end of the test range. This case also shows that the environment surrounding the building can generate considerably high RMS responses even at wind conditions that are normally safe. Which justifies the need for active control at all wind conditions. The maximum RMS response is obtained at $AOA = 90°$ for $V_r > 8.7$. This coincides with findings in the literature [28]. At $V_r = 9.7$, the neutral position response surpasses the worst plate orientations found during training. These extreme vibration levels caused some of the model columns to fail from fatigue at $V_r = 10.1$. The failed columns were later replaced, and no plate optimization was performed at this velocity or beyond. Fig. 11 also shows that in many cases, certain plate orientations maximize the RMS accelerations. This justifies the need for actively controlled aerodynamic modifications because static modifications may have a considerably negative contribution in unforeseen flow conditions. The maximum reduction obtained in the RMS acceleration sum (Eq. (1)) is 81%, 41% and 95% for the 0°, 56° and 90° directions, respectively. This major reduction underlines the overall effectiveness of the cyber–physical building system.

Fig. 12 illustrates the prediction performance of the predictor MLP which was trained using the IOT procedure. The average

absolute error in the prediction is only 0.3% the maximum RMS sum and the *R*-squared value is 0.9985. The small relative error and the high *R*-squared value mean that the trained MLP is suitable for online control of the system, as discussed in the next section. Also, due to the simultaneous optimization and training nature of the IOT procedure, most of the training points exist at the low end of RMS sum values, as shown in the figure.

4.2. Optimum performance

Fig. 13 compares the timeseries of the normalized 3-DOF accelerations of the scaled model obtained using the best and the worst plate angle combinations for each wind direction. The speed at which the plot is generated for each direction has the maximum RMS acceleration in Fig. 11 to clearly demonstrate the effect of the plates. The reduction is considerable at $AOA = 56°$ and major at both $AOA = 0°, 90°$ which agrees with the RMS acceleration results in Fig. 11. Additionally, Fig. 14 shows the corresponding along-wind acceleration PSDs for each time series. For the cases without buildings upstream (0° and 90°), the minimum acceleration response is associated with a shift of the peak frequency away from the structural natural frequencies indicated on the figure. For the case with upstream buildings (56°), the turbulence-induced wind forces on the principal model are distributed over a broader band of frequencies compared to the relatively narrowband vortex-induced forces that are most prominent for 0° and 90° cases. Also, in this configuration, plate number 4 is completely blocked by the building, which reduces its wind control authority. These factors help explain why the controller reduces the RMS response by only 41% for this case as opposed to 80%–90% for the other two cases. While the current DAA configuration may still be more effective for other surrounding environments, future studies involving a higher number of DAAs on the building's perimeter are being considered.

4.3. Control response time

Fig. 15 plots the acceleration time series of all 3 DOFs continuously before and after the plate angles were changed from the worst to the best configuration (at $AOA = 90°$ and $V_r = 9.7$). The figure was obtained by keeping the plates at a known poor configuration for a given wind condition and keeping the controller inactive for 60 s. This allowed large magnitude oscillations to develop. Then, the controller was activated, and it rotated the plates to the optimum configuration. Acceleration and plate position data was collected throughout the experiment. The figure also shows the running RMS accelerations calculated using a sliding window width of 2 s. The acceleration amplitude for rotation (dominant DOF) decreases by 33%, 61% and 90% after 1.1, 3.4 and 9.8 s, respectively. These reductions constitute major improvements in the model's WIV response. Additionally, for a deployed system, the plates will be actuated as soon as the adverse wind condition is encountered rather than waiting as was done for this demonstration. In other words, with the controller continuously activated, accelerations would not have a chance to reach these high values and the DAA actuation would require less time. At the 1/33 time scale listed in Table 2, the response time of 1.1 s corresponds to 36.3 s for the full-scale building. It is known that wind gusts typically last for less than 20 s, while squalls can continue for minutes at a time [34,35]. The proximity of the response time to the wind event time scales establishes the applicability of the proposed four-plate DAA system to mitigate WIV. However, to account for different environments and wind conditions, more advanced predictive techniques for wind condition monitoring are being considered for future studies.

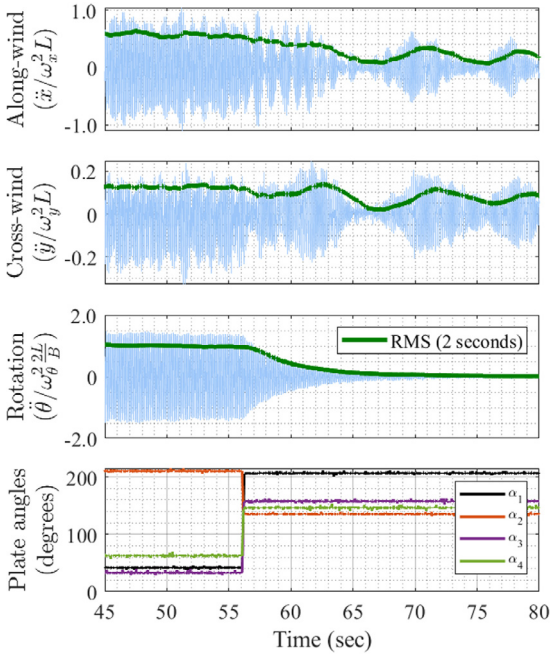

Fig. 15. Reduction of building accelerations due to changing the plate angles to the optimum values ($AOA = 90°$, $V_r = 9.7$). The IOT-based controller was inactive until $t = 56$ s for this demonstration.

5. Conclusions

An iterative optimum training (IOT) technique that can be used to simultaneously optimize and predict the behavior of nonlinear multimodal systems was presented. The technique integrates deep neural networks (DNNs) and genetic algorithms (GAs) to balance and enhance its exploitation and exploration abilities. IOT has no stall mechanism because the training samples are expanded until convergence. A benchmark of the technique showed that it can obtain the global optimum parameters using a relatively smaller number of samples or experiments, without compromising the solution quality or adding significant complexity. The technique was later utilized to generate a distributed aerodynamic actuator (DAA) controller to minimize WIV in an aeroelastic building model. The controller is based on the outputs of the IOT procedure including the trained multi-layer perceptron (MLP) network. Wind tunnel experiments of a 1:400 scale cyber–physical aeroelastic building model having 4 plates attached to its corners as DAAs were used to perform the training. The scaled model was designed using a GA procedure to guarantee the linearity of its mode shapes and generate acceptable natural frequency ratios. The model was tested at three critical wind directions (*AOA*): 0°, 56° and 90° at reduced velocities ranging from 7–11. Only the 56° direction had upstream scaled rigid buildings installed during testing to create high turbulence interference conditions. The following conclusions were obtained from the wind tunnel experiments:

1- A reduction of 41%–95% in RMS acceleration was achieved by using plate angle combinations determined from the IOT procedure across various wind conditions. The maximum reduction was obtained at $AOA = 90°$.
2- Depending on the wind condition, some plate orientations maximized the RMS response which justifies the need for actively controlled rather than static aerodynamic modifications.

3- In the frequency domain, the RMS reduction was often associated with a diversion of the wind force dominant frequencies away from the structural natural frequencies of the model.
4- The MLP generated from the IOT procedure predicted the RMS acceleration response of the building with an average absolute error of only 0.3% of the maximum RMS acceleration sum with an R-squared value of 0.9985, indicating its suitability for online control.
5- At $AOA = 90^{\circ}$ and a reduced velocity $V_r = 9.7$, engaging the IOT-based controller reduced the rotational acceleration amplitude by up to 90% at steady-state and up to 33% in as little as 1.1 s, which establishes the feasibility of the system to mitigate vibration caused by wind events for the full-scale building.

The findings of this research justify further studies involving advanced predictive wind condition monitoring techniques and additional DAA modules to further enhance practicality and multifunctionality. The benchmark comparisons and experimental results show that the IOT procedure is effective in predicting and optimizing nonlinear multimodal non-separable systems, such as the presented cyber–physical aeroelastic model.

CRediT authorship contribution statement

Khalid M. Abdelaziz: Methodology, Software, Validation, Formal analysis, Investigation, Writing – original draft, Visualization. **Jared D. Hobeck:** Conceptualization, Methodology, Software, Validation, Resources, Writing – review & editing, Supervision, Project administration, Funding acquisition.

Declaration of competing interest

The authors declare that they have no known competing financial interests or personal relationships that could have appeared to influence the work reported in this paper.

Acknowledgments

This material is based upon work supported by the National Science Foundation, United States under Grant Number CMMI-1826364. Many thanks to Dr. Warren N. White and the K-State wind power team for providing access to the wind-tunnel used in the experiments. Many thanks to Dr. Dong Lin, Mr. Guang Lin and Mr. Tyler Albright for making their 3D printing machines available for this research.

References

[1] G. Parkinson, Phenomena and modelling of flow-induced vibrations of bluff bodies, Prog. Aerosp. Sci. 26 (1989) 169–224, http://dx.doi.org/10.1016/0376-0421(89)90008-0.
[2] J.D. Hobeck, D.J. Inman, The jd number: An empirical constant for predicting dual cantilever flutter velocity, Appl. Phys. Lett. 106 (2015) 244103, http://dx.doi.org/10.1063/1.4922876.
[3] J.D. Hobeck, D.J. Inman, Dual cantilever flutter: Experimentally validated lumped parameter modeling and numerical characterization, J. Fluids Struct. 61 (2016) 324–338, http://dx.doi.org/10.1016/j.jfluidstructs.2015.11.018.
[4] A. Sharma, H. Mittal, A. Gairola, Mitigation of wind load on tall buildings through aerodynamic modifications: Review, J. Build. Eng. 18 (2018) 180–194, http://dx.doi.org/10.1016/j.jobe.2018.03.005.
[5] K. Amini, S.M. Mortazavi, E. Rezaian, A.F. Najafi, Numerical investigation on the convection heat transfer and drag reduction by utilizing the designed flow controlling blades on a smart sustainable house, Energy Effic. 12 (2018) 757–776, http://dx.doi.org/10.1007/s12053-018-9706-9.
[6] K.M. Abdelaziz, A. Alipour, J.D. Hobeck, A smart façade system controller for optimized wind-induced vibration mitigation in tall buildings, J. Wind Eng. Ind. Aerodyn. 212 (2021) 104601, http://dx.doi.org/10.1016/j.jweia.2021.104601.
[7] A. Elshaer, G. Bitsuamlak, A.E. Damatty, Enhancing wind performance of tall buildings using corner aerodynamic optimization, Eng. Struct. 136 (2017) 133–148, http://dx.doi.org/10.1016/j.engstruct.2017.01.019.
[8] U.F. Tang, K.C.S. Kwok, Interference excitation mechanisms on a 3D of aeroelastic CAARC building model, J. Wind Eng. Ind. Aerodyn. 92 (2004) 1299–1314, http://dx.doi.org/10.1016/j.jweia.2004.08.004.
[9] B. Kim, K.T. Tse, Pod analysis of aerodynamic correlations and wind-induced responses of two tall linked buildings, Eng. Struct. 176 (2018) 369–384, http://dx.doi.org/10.1016/j.engstruct.2018.09.013.
[10] J. Xie, X.-y. Yang, Exploratory study on wind-adaptable design for super-tall buildings, Wind Struct. 29 (2019) 489–497, http://dx.doi.org/10.12989/was.2019.29.6.489.
[11] Q. Yang, Z. Liu, Y. Hui, Z. Li, Modification of aerodynamic force characteristics on high-rise buildings with arrangement of vertical plates, J. Wind Eng. Ind. Aerodyn. 200 (2020) 104155, http://dx.doi.org/10.1016/j.jweia.2020.104155.
[12] D. Li, A.D. Ronch, G. Chen, Y. Li, Aeroelastic global structural optimization using an efficient CFD-based reduced order model, Aerosp. Sci. Technol. 94 (2019) 105354, http://dx.doi.org/10.1016/j.ast.2019.105354.
[13] K.M. Abdelaziz, J.D. Hobeck, Developing a smart Façade system controller for wind-induced vibration mitigation in tall buildings ASME 2019 conference on smart materials, Adapt. Struct. Intell. Syst. (2019) http://dx.doi.org/10.1115/smasis2019-5674.
[14] C.P. Fagley, D. Broadbent, J. Seidel, T.E. McLaughlin, Stall Flutter Prediction and Experimental Verification using a Cyber-Physical Wing 55th AIAA Aerospace Sciences Meeting, 2017, http://dx.doi.org/10.2514/6.2017-1416.
[15] M.L. Whiteman, P.L. Fernández-Cabán, B.M. Phillips, F.J. Masters, J.A. Bridge, J.R. Davis, Multi-objective optimal design of a building envelope and structural system using cyber-physical modeling in a wind tunnel, Front. Built Environ. 4 (2018) http://dx.doi.org/10.3389/fbuil.2018.00013.
[16] P.L. Fernández-Cabán, M.L. Whiteman, B.M. Phillips, F.J. Masters, J.R. Davis, J.A. Bridge, Cyber-physical design and optimization of tall building dynamics using aeroelastic wind tunnel modeling, J. Wind Eng. Ind. Aerodyn. 198 (2020) 104092, http://dx.doi.org/10.1016/j.jweia.2020.104092.
[17] Y.D. Sergeyev, D.E. Kvasov, M.S. Mukhametzhanov, On the efficiency of nature-inspired metaheuristics in expensive global optimization with limited budget, Sci. Rep. 8 (2018) http://dx.doi.org/10.1038/s41598-017-18940-4.
[18] R. Paulavičius, Y.D. Sergeyev, D.E. Kvasov, J. Žilinskas, Globally-biased BIRECT algorithm with local accelerators for expensive global optimization, Expert Syst. Appl. 144 (2020) 113052, http://dx.doi.org/10.1016/j.eswa.2019.113052.
[19] R.T. Haftka, D. Villanueva, A. Chaudhuri, Parallel surrogate-assisted global optimization with expensive functions – a survey, Struct. Multidiscip. Optim. 54 (2016) 3–13, http://dx.doi.org/10.1007/s00158-016-1432-3.
[20] R.G. Regis, C.A. Shoemaker, A stochastic radial basis function method for the global optimization of expensive functions, INFORMS J. Comput. 19 (2007) 497–509, http://dx.doi.org/10.1287/ijoc.1060.0182.
[21] K.M. Abdelaziz, K. Hamza, M. El-Morsi, A.O. Nassef, S.M. Metwalli, K. Saitou, Optimum solar humidification–dehumidification desalination for microgrids and remote area communities, J. Sol. Energy Eng. 138 (2016) http://dx.doi.org/10.1115/1.4032477.
[22] L. Morales, J. Aguilar, A. Rosales, D. Chávez, P. Leica, Modeling and control of nonlinear systems using an adaptive LAMDA approach, Appl. Soft Comput. 95 (2020) 106571, http://dx.doi.org/10.1016/j.asoc.2020.106571.
[23] J. Dasgupta, J. Sikder, D. Mandal, Modeling and optimization of polymer enhanced ultrafiltration using hybrid neural-genetic algorithm based evolutionary approach, Appl. Soft Comput. 55 (2017) 108–126, http://dx.doi.org/10.1016/j.asoc.2017.02.002.
[24] A. Márquez-Nolasco, R.A. Conde-Gutiérrez, J.A. Hernández, A. Huicochea, J. Siqueiros, O.R. and Pérez, Optimization and estimation of the thermal energy of an absorber with graphite disks by using direct and inverse neural network, J. Energy Res. Technol. 140 (2017) http://dx.doi.org/10.1115/1.4036544.
[25] R.A. Conde-Gutiérrez, U. Cruz-Jacobo, A. Huicochea, S.R. Casolco, J.A. Hernández, Optimal multivariable conditions in the operation of an absorption heat transformer with energy recycling solved by the genetic algorithm in artificial neural network inverse, Appl. Soft Comput. 72 (2018) 218–234, http://dx.doi.org/10.1016/j.asoc.2018.08.008.
[26] H.-X. Huang, J.-C. Li, C.-L. Xiao, A proposed iteration optimization approach integrating backpropagation neural network with genetic algorithm, Expert Syst. Appl. 42 (2015) 146–155, http://dx.doi.org/10.1016/j.eswa.2014.07.039.
[27] J.R. Noriega, H. Wang, A direct adaptive neural-network control for unknown nonlinear systems and its application, IEEE Trans. Neural Netw. 9 (1998) 27–34, http://dx.doi.org/10.1109/72.655026.
[28] F. Hou, P.P. Sarkar, Aeroelastic model tests to study tall building vibration in boundary-layer and tornado winds, Eng. Struct. 207 (2020) 110259, http://dx.doi.org/10.1016/j.engstruct.2020.110259.
[29] D.-A. Clevert, T. Unterthiner, S. Hochreiter, Fast and Accurate Deep Network Learning By Exponential Linear Units (ELUs), 2016.

[30] D.P. Kingma, J. Ba, Adam: A Method for Stochastic Optimization, 2017.
[31] M. Clerc, The Swarm and the Queen: Towards a Deterministic and Adaptive Particle Swarm Optimization Proceedings of the 1999 Congress on Evolutionary Computation-CEC99 (Cat. No. 99TH8406), 1999, http://dx.doi.org/10.1109/cec.1999.785513.
[32] Wind Tunnel Studies of Buildings and Structures, American Society of Civil Engineers, 1999, Available, DOI:10.1061/9780784403198.
[33] G. Frison, A.M. Marra, G. Bartoli, R. Scotta, Full-aeroelastic model of CAARC building: Iterative design procedure and wind tunnel tests, in: Lecture Notes in Civil Engineering, Springer International Publishing, 2019, Available, DOI:10.1007/978-3-030-12815-9_25.
[34] U. S. Department of Commerce, National Weather Service, 2020, [Online], Available: http://www.noaa.gov.
[35] American Meteorological Society, 2020, [Online], Available: www.ametsoc.org.